Monthly Notices
of the
ROYAL ASTRONOMICAL SOCIETY

MNRAS **494,** 2244–2253 (2020)
Advance Access publication 2020 March 20

doi:10.1093/mnras/staa777

Jansky VLA observations of synchrotron emitting optical hotspots of 3C 227 and 3C 445 radio galaxies

M. Orienti,[1]★ G. Migliori,[1,2] G. Brunetti,[1] H. Nagai,[3] F. D'Ammando,[1] K.-H. Mack[1] and M. A. Prieto[4]

[1]*Istituto di Radioastronomia – INAF, Via P. Gobetti 101, I-40129 Bologna, Italy*
[2]*Dipartimento di Fisica e Astronomia, Università di Bologna, Via Gobetti 93/2, I-40129 Bologna, Italy*
[3]*National Astronomical Observatory of Japan, Osawa 2-21-1, Mitaka, Tokyo 181-8588, Japan*
[4]*Instituto de Astrofísica de Canarias, c/ Vía Láctea s/n, E-38205 La Laguna (Tenerife), Spain*

Accepted 2020 March 17. Received 2020 March 17; in original form 2019 November 27

ABSTRACT

We report results on deep Jansky Very Large Array (VLA) A-configuration observations at 22 GHz of the hotspots of the radio galaxies 3C 227 and 3C 445. Synchrotron emission in the optical on scales up to a few kpc was reported for the four hotspots. Our VLA observations point out the presence of unresolved regions with upper limit to their linear size of about 100 pc. This is the first time that such compact components in hotspots have been detected in a mini-sample, indicating that they are not a peculiar characteristic of a few individual hotspots. The polarization may reach values up to 70 per cent in compact (about 0.1 kpc scale) regions within the hotspot, indicating a highly ordered magnetic field with size up to a hundred parsecs. On larger scales, the average polarization of the hotspot component is about 30–45 per cent, suggesting the presence of a significant random field component, rather than an ordered magnetic field. This is further supported by the displacement between the peaks in polarized intensity and in total intensity images that is observed in all the four hotspots. The electric vector position angle is not constant, but changes arbitrarily in the central part of the hotspot regions, whereas it is usually perpendicular to the total intensity contours of the outermost edge of the hotspot structure, likely marking the large-scale shock front. The misalignment between X-ray and radio-to-optical emission suggests that the former is tracing the current particle acceleration, whereas the latter marks older shock fronts.

Key words: acceleration of particles – polarization – radiation mechanisms: non-thermal – radio continuum: galaxies.

1 INTRODUCTION

Hotspots are bright and compact regions that are usually observed at the edge of powerful Fanaroff–Riley type II radio galaxies (Fanaroff & Riley 1974). In the standard scenario, hotspots represent the working surface of the supersonic jets produced by an active galactic nucleus (AGN). In this region both a bow-shock and a reverse shock are present, being the latter responsible for the acceleration of the particles that radiate in the hotspot. Although hotspots mainly radiate at radio wavelengths, there is a growing evidence that many of them can emit in infrared (IR)/optical band and up to X-rays (e.g. Meisenheimer, Yates & Röser 1997; Hardcastle et al. 2004; Kataoka & Stawarz 2005; Mack et al. 2009; Werner et al. 2012; Isobe et al. 2017). However, there seems to be a dichotomy in the radiation mechanism responsible for X-ray emission between high-power ($L_{1.4\mathrm{GHz}} > 10^{25}$ W Hz^{-1}) and low-power hotspot (Hardcastle et al. 2004). X-ray emission in high-power hotspots is well explained as synchrotron self-Compton (SSC, Harris, Carilli & Perley 1994; Werner et al. 2012), whereas in low-power hotspots an additional contribution from synchrotron radiation from a highly energetic electron population is expected to be present (e.g. Hardcastle et al. 2016).

Given the anticorrelation between the synchrotron radiative lifetime, τ, and the Lorentz factor of the relativistic electrons $\gamma > 10^{7-8}$, the detection of synchrotron X-ray emission from a hotspot implies that particle acceleration is currently taking place owing to the short radiative lifetime of the electrons involved ($\tau \propto 1/\gamma$). Using Very Long Baseline Array (VLBA) observations, Tingay et al. (2008) suggested that X-ray emission in the western hotspot of Pictor A may be produced by synchrotron emission from compact pc-scale transient regions of enhanced magnetic field. The discovery of flux variability up to 10 per cent level in the hotspot of Pictor A strongly supports this scenario (Hardcastle et al. 2016). The time-scale of the temporal variability corresponds to spatial scales much smaller than the physical size of the hotspot, suggesting that a

★ E-mail: orienti@ira.inaf.it

significant contribution to the X-ray emission comes from one or more very compact regions.

The detection by the Very Large Telescope (VLT) of kpc-scale diffuse near-IR (NIR) and optical synchrotron emission from hotspots provides complimentary information on the complexity of particle acceleration and transport in radio hotspots (Mack et al. 2009). In these cases, a combination of multiple and intermittent compact acceleration sites and stochastic (e.g. Fermi-II type) acceleration mechanisms have been proposed to circumvent the tension between the short lifetime of the optical synchrotron emitting electrons and the extension of the emitting region (e.g. Prieto, Brunetti & Mack 2002; Orienti et al. 2012). This idea has been recently supported by full-polarization Atacama Large Millimeter Array (ALMA) observations of the hotspot 3C 445 South where bright and highly polarized components are enshrouded by diffuse unpolarized emission (Orienti et al. 2017).

In this paper we present the results on new A-configuration Very Large Array (VLA) observations at 22 GHz in full polarization of the hotspots of the radio galaxies 3C 227 and 3C 445 with the aim of understanding how strong shocks are distributed in the hotspot regions. These hotspots are part of the low-power ($P_{1.4\,\mathrm{GHz}} < 10^{25}$ W Hz^{-1}) hotspot sample selected by Brunetti et al. (2003), and target of VLT *K*-band observations. NIR emission is detected in each hotspot (Mack et al. 2009) and is extended on kpc-scale (Orienti et al. 2012; Migliori et al., in preparation). All the hotspots have X-ray emission (e.g. Hardcastle, Croston & Kraft 2007; Perlman et al. 2010; Orienti et al. 2012), with the exception of 3C 445 North which has only a tentative *Chandra* detection (Mingo et al. 2017).

The high resolution of our VLA observations allows us to pick up particle acceleration sites down to scales of few tens parsecs. The availability of polarization information enables the study of the magnetic field structure on scales that have never been investigated in hotspots with such details. This paper is organized as follows: in Sections 2 and 3 we present the observations and data analysis; results are reported in Section 4 and discussed in Section 5. A brief summary is presented in Section 6.

Throughout this paper, we assume the following cosmology: $H_0 = 71$ km s^{-1} Mpc^{-1}, $\Omega_\mathrm{M} = 0.27$, and $\Omega_\Lambda = 0.73$, in a flat Universe. The spectral index α is defined as $S(\nu) \propto \nu^{-\alpha}$. In all the images, North is up and West is right. 3C 227 and 3C 445 are at redshift $z = 0.086$ and 0.055, respectively. At the redshift of the sources, 1 arcsec corresponds to 1.62 and 1.07 kpc for 3C 227 and 3C 445, respectively.

2 RADIO OBSERVATIONS

Full-polarization VLA observations in A-configuration for 3C 227 and 3C 445 were carried out on 2018 March 5 and May 18, respectively (project code 18A-087). The observations have a total band width of 8 GHz divided into 4 × 2-GHz basebands centred on 19, 21, 23, and 25 GHz. The target on-source observing time is about 30 min, for a total observing time of 7 h. The absolute amplitude scale and the absolute polarization angle were calibrated using the flux density scale from Perley & Butler (2013a) and the polarization information from Perley & Butler (2013b) for the calibrator 3C 286. Bandpass was calibrated using the calibrator J0927+3902 (4C 39.25) and J2253+1608 (3C 454.3) for 3C 227 and 3C 445, respectively. In addition, the instrumental polarization (D-terms) was calibrated using the unpolarized sources J0713+4349 and J2355+4950 for 3C 227 and 3C 445, respectively.

Calibration and data reduction were done using Common Astronomical Software Applications (CASA) version 4.7.0. The uncertainty on the flux density due to amplitude calibration errors σ_cal was estimated by checking the scatter of the amplitude gain factors, and turned out to be less than 3 per cent. This value is in agreement with the errors that are usually given by Perley & Butler (2013a) from the long-term monitoring program.

Final images have a resolution of about 0.08 × 0.07 arcsec^2 and 0.11 × 0.07 arcsec^2 for 3C 227 and 3C 445, respectively, and an rms of 6 μJy beam^{-1} in Stokes I, Q, and U. Images in Stokes Q and U have been used to produce the polarization intensity, polarization angle, fractional polarization, and the associated error images. Blanking on the fractional polarization image was done by clipping the pixels of the input images with values below three times the rms measured on the off-source image plane. The uncertainty on the polarization angle is about 4 deg.

For all the sources we also produced images (Stokes IQU), using the natural weighting algorithm which are most sensitive to extended emission. The flux density reported in Table 1 refers to natural weighting images.

Table 1. Total intensity and polarization properties of the hotspots. Column 1: hotspot name; Column 2: hotspot component; Column 3: total intensity flux density at 22 GHz; and Columns 4 and 5: polarized flux density and fractional polarization at 22 GHz, respectively.

Hotspot	Comp.	I (mJy)	P (mJy)	m (per cent)
3C 227 West	E	27.42 ± 0.84	11.56 ± 0.39	42 ± 1
	N	3.51 ± 0.11	1.47 ± 0.06	42 ± 1
	S	3.80 ± 0.12	1.85 ± 0.06	48 ± 1
	W	6.44 ± 0.25	3.55 ± 0.18	55 ± 3
3C 227 East	HS	8.15 ± 0.28	2.79 ± 0.15	34 ± 2
	K	0.59 ± 0.04	0.27 ± 0.04	45 ± 8
	N	3.40 ± 0.16	1.76 ± 0.14	52 ± 4
	S	9.33 ± 0.35	5.31 ± 0.27	57 ± 3
	V	14.59 ± 0.51	10.58 ± 0.41	72 ± 2
3C 445 North	Tot	16.67 ± 0.50	7.42 ± 0.24	44 ± 6
3C 445 South	Tot	38.10 ± 1.15	12.24 ± 0.40	32 ± 1
	E	14.24 ± 0.43	5.18 ± 0.16	36 ± 1
	W	2.92 ± 0.09	0.79 ± 0.04	27 ± 1
	S	0.90 ± 0.03	0.37 ± 0.02	41 ± 2

3 *CHANDRA* OBSERVATIONS

X-ray studies of the hotspots of 3C 227 and 3C 445 have been presented in several papers (Hardcastle et al. 2007; Perlman et al. 2010; Orienti et al. 2012; Mingo et al. 2017; Migliori et al., in preparation). Here, we retrieved and analysed the archival *Chandra* observations with the goal of comparing the X-ray morphology with the structures observed in total intensity and polarization at 22 GHz.

The X-ray data analysis was performed with the Chandra Interactive Analysis of Observation (CIAO) 4.9 software (Fruscione et al. 2006) using the calibration files CALDB version 4.7.7. We ran the `chandra_repro` reprocessing script, that performs all the standard analysis steps.

We checked and, when necessary, filtered the data for the time intervals of background flares. We adjusted the astrometry of the X-ray images by shifting the X-ray centroid of the cores to the radio positions and verified the correct alignment by comparison with the positions of background sources with IR and optical catalogues (2MASS Point Source Catalog and USNO B1.0, Skrutskie et al. 2006). In this way, we estimated <0.15 arcsec pointing accuracy.

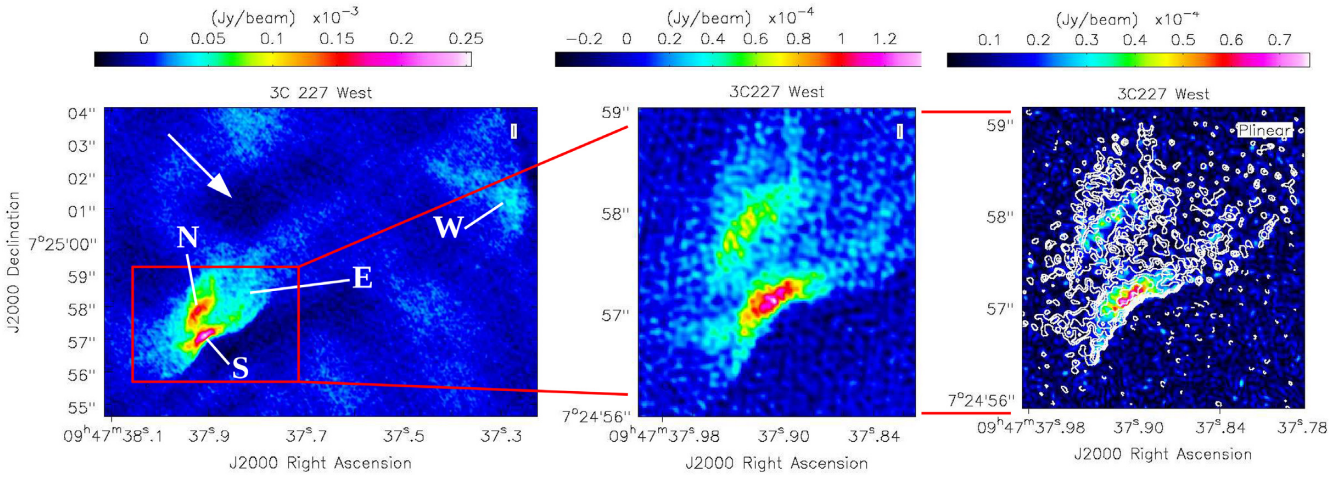

Figure 1. Left-hand panel: total intensity VLA image at 22 GHz of the hotspot complex 3C 227 West obtained with natural weighting. The arrow indicates the direction of the jet. Central panel: zoom of the Eastern region of the hotspot 3C 227 West in total intensity obtained using Briggs weighting. Right-hand panel: zoom of the Eastern region of the hotspot 3C 227 West in total intensity (contours) overlaid with polarized intensity image. The first contour is 18 μJy beam^{-1} and corresponds to three times the off-source noise level measured on the image plane. Contours increase by a factor of $\sqrt{2}$. The colour scale is shown by the wedge at the top of each image.

3C 227 was observed twice in 2006 January (ObsIDs 7265 and 6842) in very faint (VF) mode for ∼53 ksec in total and the two observations were merged together and rebinned to a pixel size of 0.123 arcsec.

We selected the ∼46 ks observation of 3C 445 performed by *Chandra* in faint (F) mode in 2007 (ObsID 7869).[1] Given the higher number of counts, the X-ray image of 3C 445 could be rebinned to one-eighth of the native pixel size (0.0615 arcsec) in order to have a resolution roughly matching that of the VLA data.

The western hotspot of 3C 227 and the southern hotspot of 3C 445 were placed near the aim point, on the S3 chip of the ACIS-S array. Because of the angular extension of the two radio galaxies, the hotspots of the counter jets fall on a different chip and they are only weak or marginally detected in X-rays (see also Hardcastle et al. 2007; Perlman et al. 2010; Mingo et al. 2017).

4 RESULTS

Significant radio emission at 22 GHz is observed in all four hotspots targeted in the study. The total intensity flux density and the polarized flux density are extracted from the same region by selecting polygonal areas on the image plane. The values are reported in Table 1. We also derive the peak flux density and the upper limit on the deconvolved angular size of the unresolved components by performing a Gaussian fit to the source components on the image plane using the task `imfit` in CASA. The error on the total intensity and polarized flux density, σ_S, is given by $\sigma_S = \sqrt{\sigma_{\rm cal}^2 + \sigma_{\rm rms}^2}$, where $\sigma_{\rm rms} = {\rm rms} * \sqrt{N}$ and N is the number of independent beam areas through the component region, while $\sigma_{\rm cal}$ is about three per cent (see Section 2). The error on the position of peak of unresolved components is $\Delta\theta = \sqrt{\sigma_{\rm fit}^2 + \sigma_{\rm p}^2}$, where $\sigma_{\rm fit}$ is the error of the Gaussian fit, whereas $\sigma_{\rm p} = {\rm beamsize/S/N}$, where S/N is the signal-to-noise ratio and corresponds to $S_{\rm p}$/rms where $S_{\rm p}$ is the peak flux density of the component and rms corresponds to 1σ noise level. For unresolved components with high S/N $\sigma_{\rm p}$ may be very small. In this case we assume a conservative error on the component position of 1/10 of the beam size (e.g. Polatidis & Conway 2003).

Errors on the polarization parameters were computed following Fanti et al. (2001). Errors on the fractional polarization range from about 1 per cent in the brightest regions up to 40 per cent in the ridges and in the extended structures with low S/N.

In all the hotspot complexes we could detect hints of extended emission that is present in images at lower frequencies (Black et al. 1992; Leahy et al. 1997; Orienti et al. 2012), and that is mainly resolved out in our observations (largest angular size ≤2.4 arcsec). Significant polarization is observed in all the hotspot regions reaching values up to 70 per cent. A description of each hotspot is presented in the following sections.

4.1 3C 227 West

3C 227 West is a double hotspot with the eastern and western components separated by about 10 arcsec (e.g. Black et al. 1992). The western component has a size of about 3 arcsec (∼ 4.8 kpc), and is detected only in natural weighting images (Fig. 1), while it is resolved out in full-resolution images. The high angular resolution of our VLA observations could resolve the structure of the eastern component for the first time in two arc-shaped structures elongated in the SE–NW direction, and separated by about 0.75 arcsec (1.2 kpc), with the northern component in agreement with the edge of the X-ray emission (Fig. 2). The elongation of these components is roughly transverse to the direction of the jet, as it is deduced by low-resolution images (e.g. Mack et al. 2009). VLT observations suggest a similar double arc-shaped structure of the NIR emission, but the lower angular resolution prevents us from a more detailed imaging in the NIR/optical regime (Migliori et al., in preparation). The southern arc, S component in Fig. 1, is the brightest one and accounts for ∼20 per cent of the flux density of the hotspot region. The polarization and the total intensity emission have a similar structure. In the hotspot components N and S there are unresolved polarized regions with size between 75 and 100 mas,

[1]In two other epochs of observations of 3C 445 in 2009 and 2011, the pointing settings were not suitable for our study. On these occasions the use of the gratings reduced the photon counts, and the hotspots were >4 arcmin offset from the observation axis and thus severely affected by distortions of the point spread function (PSF).

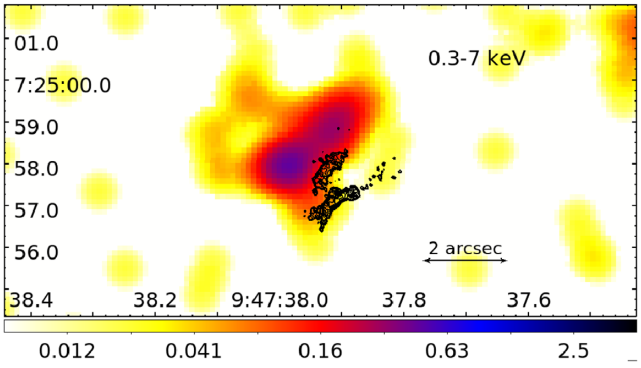

Figure 2. 0.3–7 keV *Chandra* image of the eastern component of 3C 227 West (colour-scale) overlaid with 22-GHz VLA image. The first contour is 24 μJy and contours increase by a factor of $\sqrt{2}$. The colour scale in counts per pixel is shown by the wedge at the bottom of the image.

corresponding to about 120–160 pc, and a flux density of about 35–150 μJy. There seems to be a displacement between the position of the compact components observed in total intensity and those observed in polarized emission, which accounts for about 40 $\pm$ 10 mas (65 $\pm$ 7 pc) between the total intensity peak and the polarization peak of the brightest unresolved subcomponent of the southern arc (Fig. 1, right-hand panel). The polarized emission is patchy and the observed fractional polarization ranges between 15 and 60 per cent (Fig. 3). Electric vector position angle (EVPA) is not constant across the hotspot region, ranging between 15° and 60° in component S, and between 30° and 60° in component N.

4.2 3C 227 East

This hotspot region has a complex structure. The main hotspot component is labelled HS in Fig. 4, is about 0.8 arcsec (∼1.3 kpc) in size, and accounts for 30 per cent of the emission measured on the entire hotspot complex. Component HS is resolved in several polarized subcomponents (Fig. 4, central and right-hand panels). The upper limit to their size is about 70–100 mas, corresponding to about 110–160 pc, and the flux density is about 20–50 μJy. Although the polarization and total intensity emission have a similar structure, there seems to be a displacement between the peaks of the total intensity emission and the peaks of polarized emission which accounts for 40 $\pm$ 10 mas (65 $\pm$ 7 pc) for the brightest and unresolved components, similarly to 3C 227 West. The average observed fractional polarization for component HS is about 34 per cent, but it reaches values as high as 50 per cent in the central region (Fig. 5). EVPA changes across component HS, ranging between 15° and −70° in the highly polarized structure. A bright component is observed at about 1.5 arcsec (∼2.4 kpc) to the north-west of component HS, and is labelled K in Fig. 4. Component K may trace the location where the jet bends before reaching component HS. The X-ray emission is mainly observed between component HS and K. However, the low signal-to-noise ratio precludes us from determining the precise X-ray brightness distribution (Fig. 6).

In addition to these bright components, three filaments are clearly visible in our radio images, in agreement with what was found at 3.6 cm by Black et al. (1992). A cusp-like structure, labelled V in Fig. 4, is present to the West and seems to mark the edge of the X-ray emission (Fig. 6). A deeper X-ray observation is crucial for confirming this positional correspondence. These extended structures are characterized by very high level of polarization (Table 1). This may be an indication that the total intensity structure is extended on scales larger than the largest angular size recoverable by our observations (∼ 2.4 arcsec) as also suggested by images at 3.6 cm presented in Black et al. (1992), while the polarized structures are more compact.

4.3 3C 445 North

This hotspot is about 4 arcsec in size and has an S-shaped structure elongated in the NE–SW direction, roughly transverse to the jet

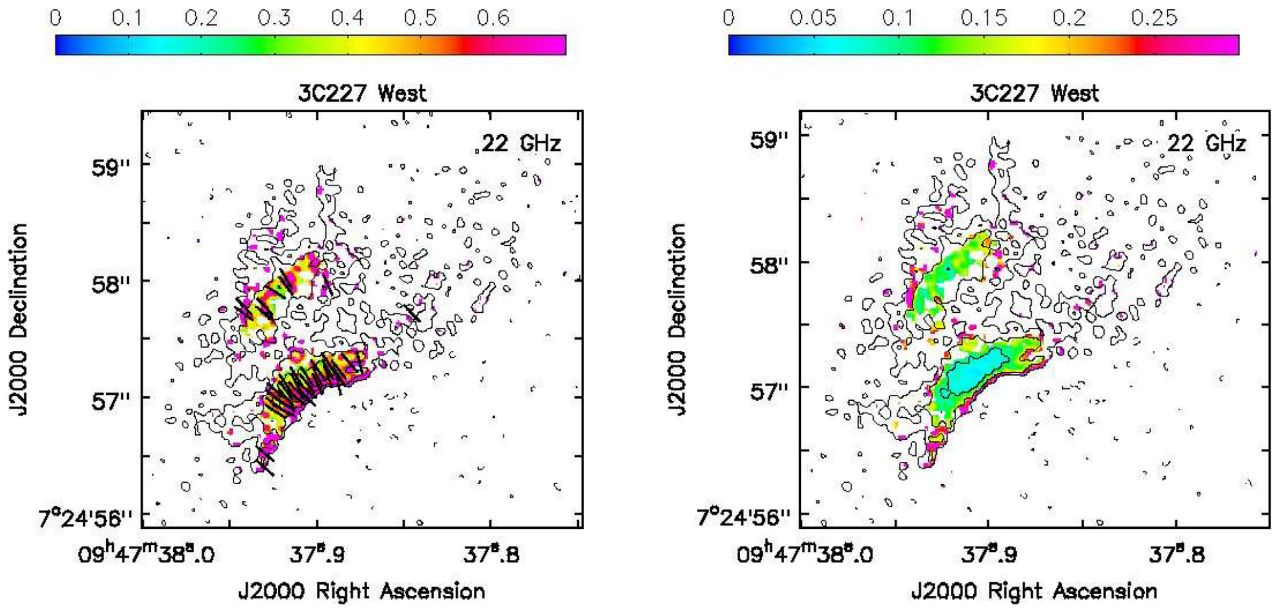

Figure 3. Fractional polarization image (left) and fractional polarization error image (right) of the hotspot 3C 227 West. The first contour is 18 μJy beam^{-1} and corresponds to three times the off-source noise level measured on the image plane. Contours increase by a factor of 2. The colour scale is shown by the wedge at the top of each image. Vectors represent the EVPA.

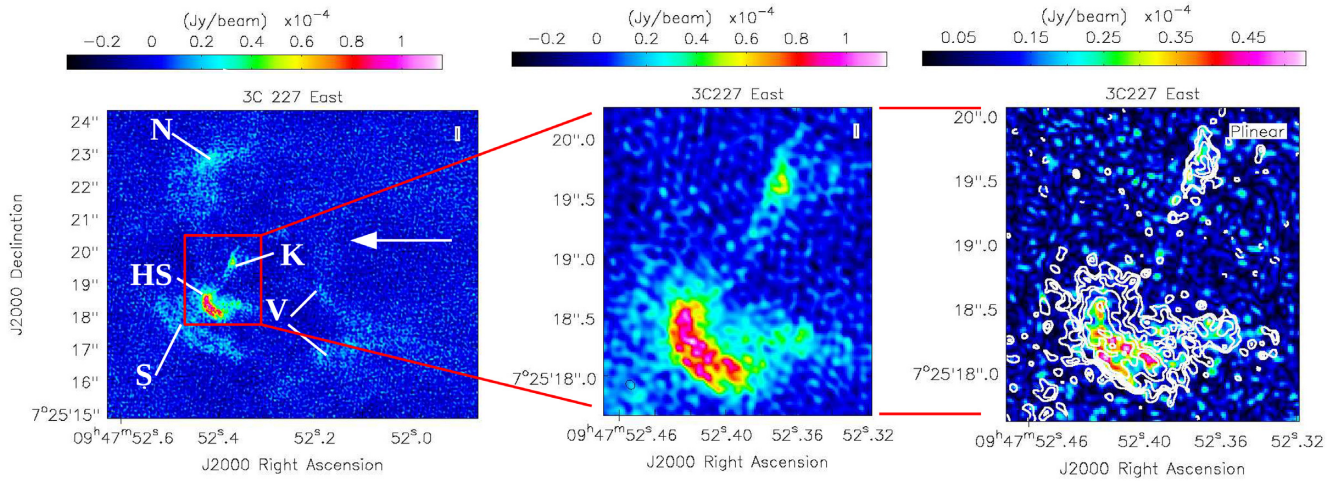

Figure 4. Left-hand panel: total intensity VLA image at 22 GHz of the hotspot complex 3C 227 East obtained with natural weighting. The arrow indicates the direction of the jet. Central panel: zoom of the main hotspot region of 3C 227 East in total intensity obtained using Briggs weighting. Right-hand panel: zoom of the main hotspot region of 3C 227 East in total intensity (contours) overlaid with polarized intensity image. The first contour is 18 μJy beam^{-1} and corresponds to three times the off-source noise level measured on the image plane. Contours increase by a factor of $\sqrt{2}$. The colour scale is shown by the wedge at the top of each image.

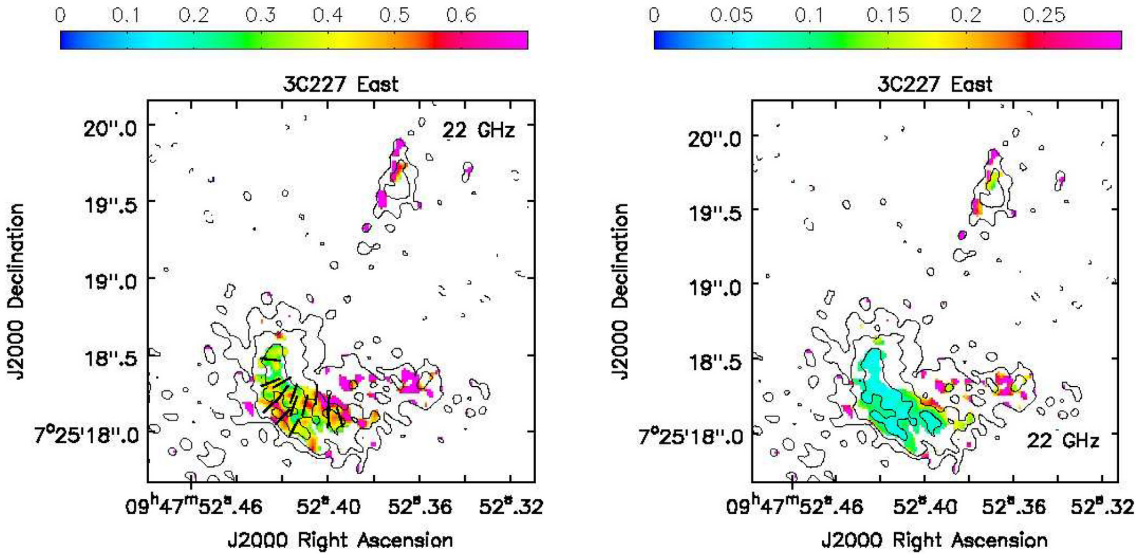

Figure 5. Fractional polarization image (left) and fractional polarization error image (right) of the hotspot 3C 227 East. The first contour is 18 μJy beam^{-1} and corresponds to three times the off-source noise level measured on the image plane. Contours increase by a factor of 2. The colour scale is shown by the wedge at the top of each image. Vectors represent the EVPA.

direction as derived from the low-resolution images presented in Mack et al. (2009). The radio emission is dominated by the central region which is resolved in several subcomponents (Fig. 7). When observed with full resolution, both the total intensity and the polarized emission are patchy with several unresolved subcomponents enshrouded by diffuse emission. The upper limit to the angular size of these subcomponents is about 70–120 mas, corresponding to a linear size of about 75–130 pc, and a flux density between 20 and 30 μJy. The total intensity structure is elongated in NS direction, while the polarized emission seems to form two roughly parallel structures oriented in the NE–SW direction, with the northern component being the brighter (Fig. 7) and accounting for roughly 10 per cent of the polarization of the entire hotspot. The average observed fractional polarization of the hotspot complex is about 44 per cent, reaching values as high as 60 per cent in the central region. The EVPA changes across the hotspot region ranging from $-32°$ to $-85°$, being locally roughly transverse to the elongation of the polarized structure and to the total intensity contours of the northern edge of the S-shaped structure (Fig. 8).

4.4 3C 445 South

This hotspot complex has an angular size of about 6 arcsec (about 6.4 kpc) and consists of two main components with an arc-shaped structure, with the eastern one in agreement with the edge of the X-ray emission (Fig. 9). The eastern component, labelled E in Fig. 10, is the brightest one and consists of about 50 per cent of the whole hotspot complex. Its structure is elongated in the east-west direction,

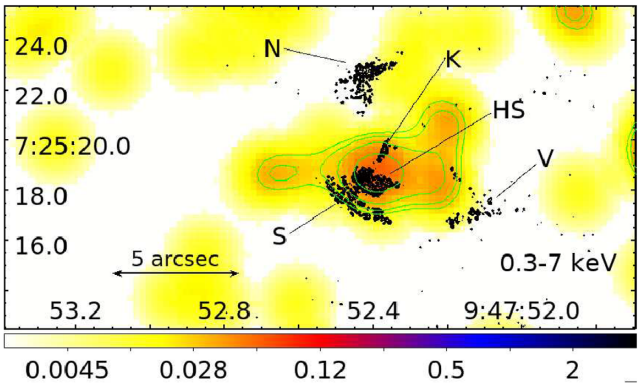

Figure 6. 0.3–7 keV *Chandra* image of 3C 227 East (colour-scale) overlaid on 22-GHz VLA image. The image is half the native *Chandra* pixel size and has been smoothed with a Gaussian filter with $\sigma = 7$. The logarithmic X-ray contours (in green) start at three times the rms noise (0.007 cts). The first contour is 18 μJy and contours increase by a factor of $\sqrt{2}$. The colour scale is shown by the wedge at the bottom of the image.

roughly transverse to the direction of the jet, as it is derived by low-resolution images (e.g. Leahy et al. 1997; Mack et al. 2009). In this hotspot component, there are several unresolved polarized subcomponents. The upper limit to their angular size is between 70 and 120 mas, corresponding to about 75 and 130 pc, and a flux density of about 20–30 μJy. The average observed fractional polarization of component E is about 36 per cent, but reaches values as high as 50 per cent. Component W is elongated in the north west-south east direction and is about 2.5 arcsec from component E in the south-west direction. The average observed polarization of component W is 27 per cent, but reaches values as high as 55 per cent (Fig. 11). The fractional polarization of both components derived in our 22-GHz observations is slightly larger than that at 97.5 GHz from ALMA observations (Orienti et al. 2017). This may be due to the better resolution of these VLA data ($\leq$0.1 arcsec) with respect to the resolution of our earlier ALMA observations ($\sim$0.5 arcsec which corresponds to $\sim$550 pc), and suggests the presence of tangled magnetic field components with angular scales that are smaller than the resolution proved by our earlier ALMA observations.

The X-ray emission is detected at the edge of the main hotspot component, likewise in 3C 227 East. The polarization and the total intensity emission have a similar structure (Fig. 11). However, the brightest component in total intensity has a relatively low polarization and is located about half-way between the two brightest components in polarized intensity (about 100 $\pm$ 10 and 70 $\pm$ 10 mas, respectively). Polarized emission is also observed in the ridge of the arc-shaped structure and in component S that is located between component E and W in the southern direction (Fig. 10). The EVPA changes across the whole hotspot region, from about -10° to -55°, while it becomes roughly perpendicular to the total intensity contours in the southern edge. Between the two main components no significant polarization is detected, with a fractional polarization below 3 per cent (Fig. 11), which is consistent with the 4 per cent upper limit that was set by ALMA observations (Orienti et al. 2017).

5 DISCUSSION

5.1 The hotspot structure and the magnetic field

Particle acceleration via strong shocks, turbulence, and/or magnetic reconnection should take place in the hotspot regions of radio galaxies. The detection of extended synchrotron optical emission confirms the presence of efficient particle acceleration distributed on kpc scales. The high resolution of our VLA observations of the hotspots in 3C 445 and 3C 227 pointed out a very complicated morphology with arc-shaped structures that could be resolved into several polarized subcomponents enshrouded by diffuse emission. These structures may trace multiple shocks and compression or regions of magnetic reconnection. The upper limit to their size ranges between 75 and 160 pc. Components with size of a few tens parsecs were already observed in other hotspots like 3C 205 (Lonsdale & Barthel 1984), 4C 41.07 (Gurvits et al. 1997), Pictor A (Tingay et al. 2008), and PKS 2153–69 (Young et al. 2005). VLA observations of Cygnus A at 43 GHz could resolve the hotspot structures in small clumps of about 0.4 kpc in size (Carilli et al.

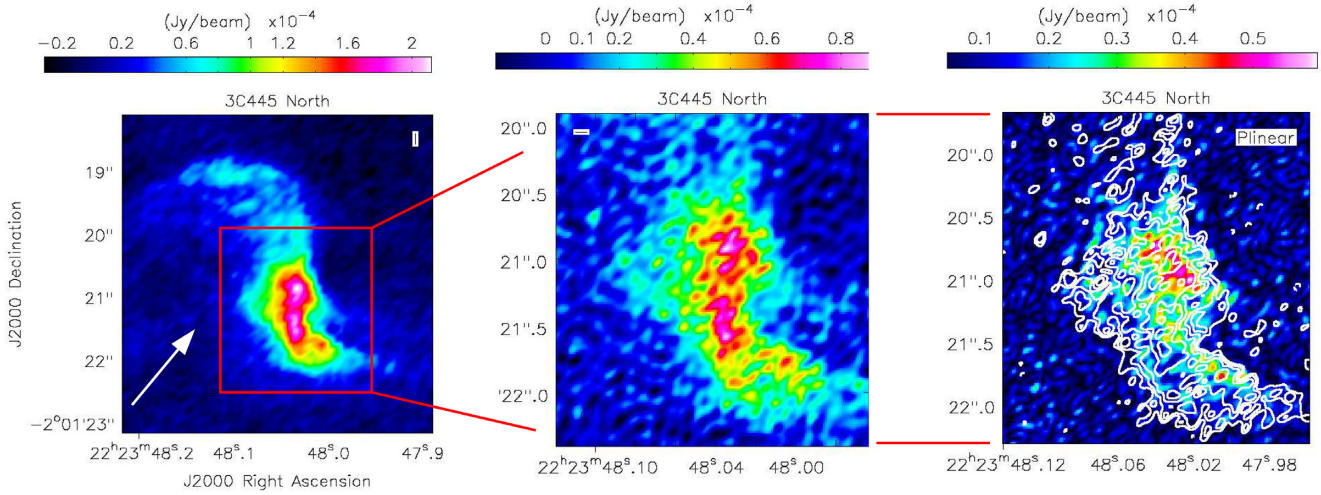

Figure 7. Left-hand panel: total intensity VLA image at 22 GHz of the hotspot complex 3C 445 North obtained with natural weighting. The arrow indicates the direction of the jet. Central panel: zoom of the central region of the hotspot 3C 445 North in total intensity obtained using Briggs weighting. Right-hand panel: zoom of the central region of the hotspot 3C 445 North in total intensity (contours) overlaid with polarized intensity image. The first contour is 18 μJy beam^{-1} and corresponds to three times the off-source noise level measured on the image plane. Contours increase by a factor of $\sqrt{2}$. The colour scale is shown by the wedge at the top of each image.

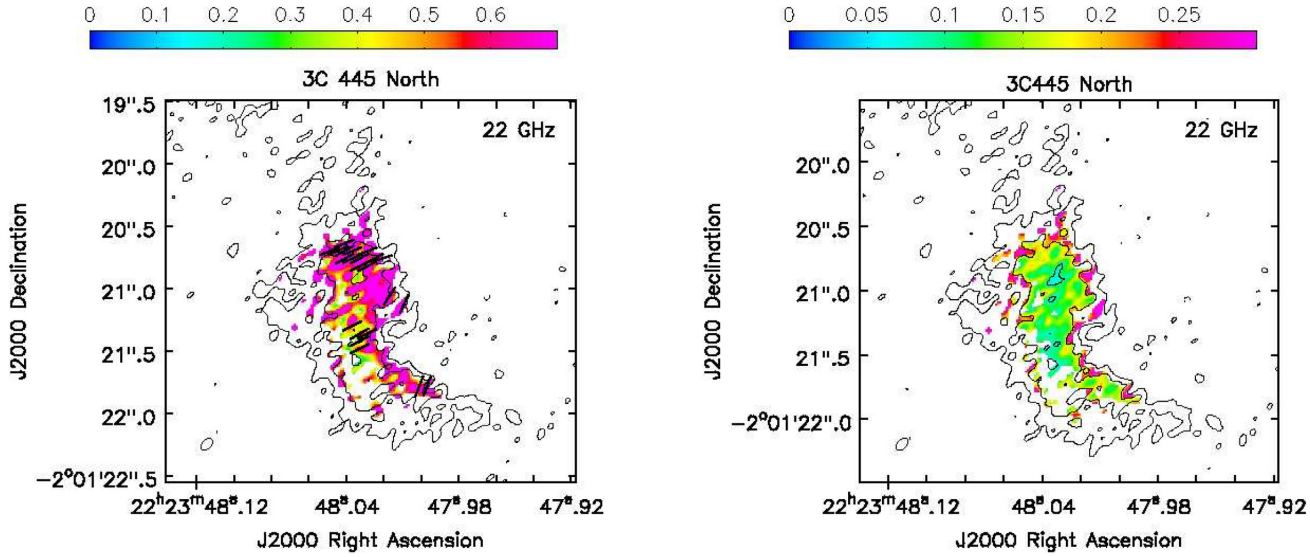

Figure 8. Fractional polarization image (left) and fractional polarization error image (right) of the hotspot 3C 445 North. The first contour is 18 μJy beam^{-1} and corresponds to three times the off-source noise level measured on the image plane. Contours increase by a factor of 2. The colour scale is shown by the wedge at the top of each image. Vectors represent the EVPA.

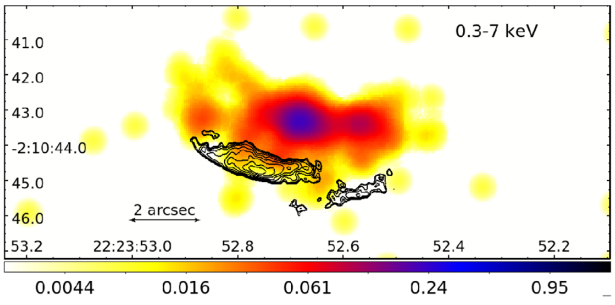

Figure 9. 0.3–7 keV *Chandra* image of 3C 445 South (colour-scale) overlaid with 22-GHz VLA image. The first contour is 18 μJy and contours increase by a factor of $\sqrt{2}$. The colour scale is shown by the wedge at the bottom of the image.

1999). Depending on their actual size, the existence of highly magnetized small clumps in the hotspot regions of Cygnus A may provide an explanation to the low-energy curvature that has been observed by the Low Frequency Array (McKean et al. 2016).

In all of the four hotspots studied here, about 10 per cent of the total flux density of the hotspot region is globally produced in compact unresolved components, whereas the majority of the emission is on larger scales. The polarized emission is characterized by several unresolved components, which may not correspond to the unresolved components observed in total intensity. In particular, in 3C 445 North, the polarized structure is different from the total intensity morphology. In this hotspot, the highly polarized components constitute about 10 per cent of the hotspot polarized emission. The polarized emission reaches a fractional polarization as high as 70 per cent, and is elongated in the NE-SW direction. On the other hand, the total intensity emission is elongated in the NS direction with the southern part being brighter in total intensity, but showing lower levels of polarization (about 20 per cent).

The complex structure of polarized and total intensity emission observed in these hotspots suggests that the magnetic field is not homogeneously distributed in the hotspot region. The fractional polarization between 30 and 45 per cent that is observed on average indicates the presence of a significant random field component. This is supported by the fact that EVPA of the different clumps varies. The polarization decreases at the boundaries between the clumps, and this may be due to vector cancellation when cells with different EVPA fall within the interferometer beam. Another piece of evidence is provided by the lower level of fractional polarization that is observed in the images produced with natural weights (whose restoring beam is ∼2.5 times larger than the beam obtained with full resolution), where the maximum fractional polarization is about 40 per cent and the polarized emission is smoothly distributed across the hotspot region. High-resolution very long baseline interferometry (VLBI) observations are crucial for constraining the size of the compact subcomponents and infer the orientation of the magnetic field on parsec scales.

The observed polarization $p_{\rm obs}$ depends on the intrinsic polarization $p_{\rm int}$ and on the number of turbulent cells N intercepted by the observing beam $A_{\rm b}$ by $p_{\rm obs} \sim p_{\rm int} N^{-1/2}$, where $N = A_{\rm b}\phi l^{-3}$ in which l is the size of the turbulent cells and ϕ is the size of the turbulent region (Beck, Berkhuijsen & Uyaniker 1999). If we consider the beam of our VLA observations and the average angular to linear scale conversion, we have that:

$$p_{\rm int} \sim 0.1 p_{\rm obs} \phi^{1/2} l^{-3/2} \quad (1)$$

In Fig. 12, we plot the intrinsic fractional polarization as a function of the size of the turbulent cells, for various values of the observed fractional polarization and assuming a total extent of the turbulent region of 1 kpc. This is an average value for the main hotspot regions of the sources studied here. For l of about 0.1–0.16 kpc, as obtained from our VLA images and from the upper limit from ALMA observations (Orienti et al. 2017), we find that the expected intrinsic fractional polarization is between 60 and 90 per cent if we consider an observed fractional polarization of about 30–45 per cent, i.e. in agreement with the average integrated value of our observations. The high value of the expected intrinsic percentage, above 70–80 per cent, suggests that the average scale size of the acceleration regions and/or magnetic field length should not be much smaller than the scale proved by our observations (∼0.1–0.16 kpc). We remark that this is an average scale size, and

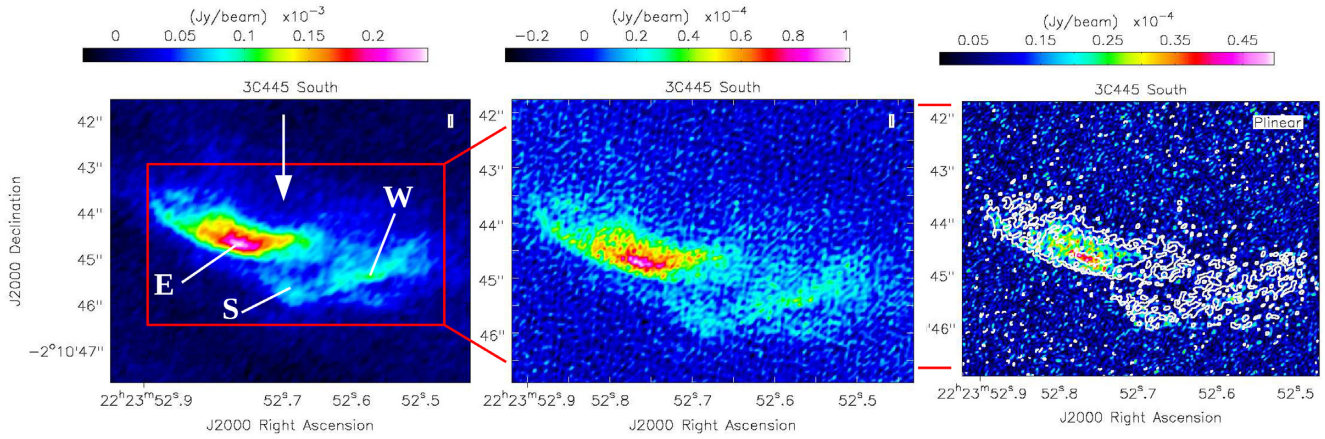

Figure 10. Left-hand panel: total intensity VLA image at 22 GHz of the hotspot complex 3C 445 South obtained with natural weighting. The arrow indicates the direction of the jet. Central panel: zoom of the central region of the hotspot 3C 445 South in total intensity obtained using Briggs weighting. Right-hand panel: zoom of the central region of the hotspot 3C 445 South in total intensity (contours) overlaid with polarized intensity image. The first contour is 18 μJy beam^{-1} and corresponds to three times the off-source noise level measured on the image plane. Contours increase by a factor of 2. The colour scale is shown by the wedge at the top of each image.

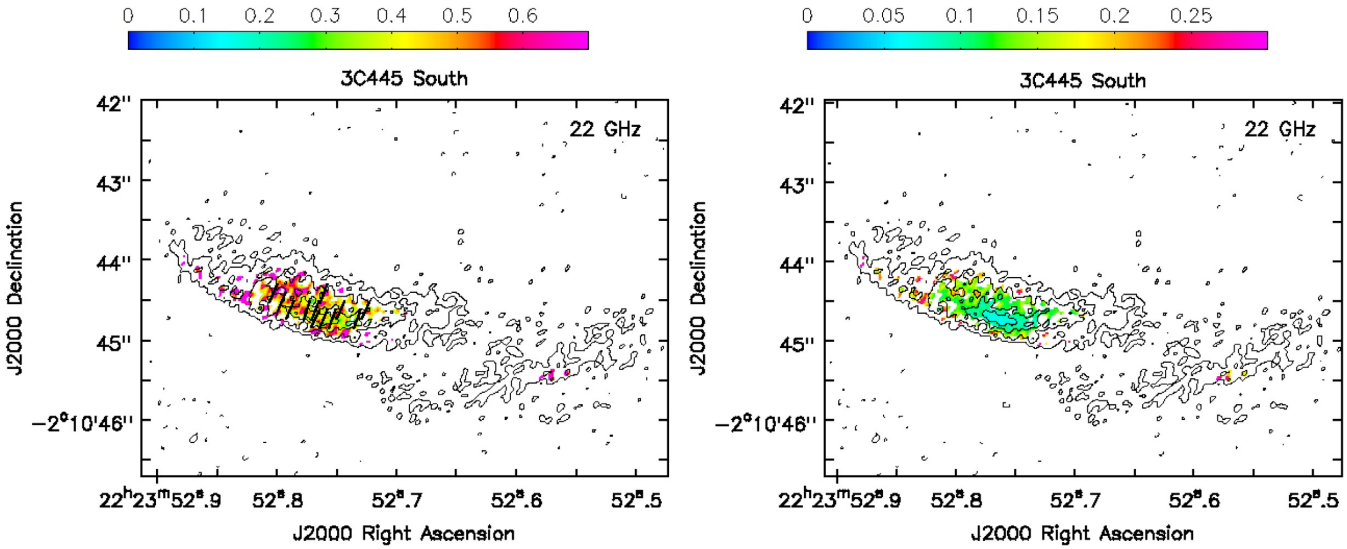

Figure 11. Fractional polarization image (left) and fractional polarization error image (right) of the hotspot 3C 445 South. The first contour is 18 μJy beam^{-1} and corresponds to three times the off-source noise level measured on the image plane. Contours increase by a factor of 2. The colour scale is shown by the wedge at the top of each image. Vectors represent the EVPA.

the presence of transient compact pc-scale components with shorter radiative lifetime cannot be excluded.

In each hotspot, the EVPA is not constant and changes arbitrarily in the central region. However, the EVPA is usually perpendicular to the total intensity contours in the outer edge of the hotspot structure, suggesting the presence of compression that makes the turbulent field tangential to the boundaries of the source (e.g. Laing 1980).

In presence of an irregular field that is subject to compression, we evaluate how the observed fractional polarization, $p_{\rm obs}$ changes as a function of the line of sight. The intrinsic fractional polarization $p_{\rm int}$ is not critically dependent on the spectral index α, with a variation of $\sim$10 per cent assuming values for α between 0.5 and 1 (Burn 1966; Laing 1980). For simplicity, and for consistency with previous studies (e.g. Laing 1980; Lonsdale & Barthel 1998), we assume $\alpha = 1$. This value is steeper than what is usually observed in hotspots. However, there seems to be a tension between the observed spectral index in hotspots and the injection spectral index which has been found to be steeper (Harwood et al. 2017). The observed fractional polarization, $p_{\rm obs}$ is:

$$p_{\rm obs} = p_{\rm int} \frac{B_o^2 \sin^2\theta}{B_o^2 \sin^2\theta + B_r^2} \quad (2)$$

where $B_o \sin\theta$ is the component of the ordered magnetic field on the plane of the sky, θ is the angle to our line of sight, and B_r is the random component of the magnetic field with scale length comparable to the interferometer beam. In Fig. 13, we plot the observed fractional polarization as a function of θ for various values of the ratio B_o/B_r and assuming an intrinsic polarization $p_{\rm int} =$ 70 per cent, i.e. about the central value in the estimated range from equation (1). The large percentage of polarization reaching 55–70 per cent that is observed in the unresolved compact components in each hotspot, indicates that in these regions the magnetic field is organized on scales of up to a hundred pc. If the field random component is equal to or higher than the ordered component, low

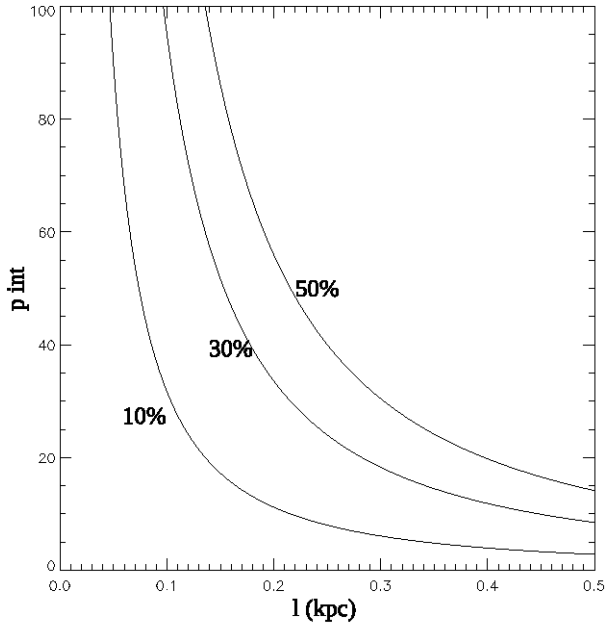

Figure 12. Intrinsic fractional polarization as a function of the linear size of the turbulent cells for different values of the observed fractional polarization.

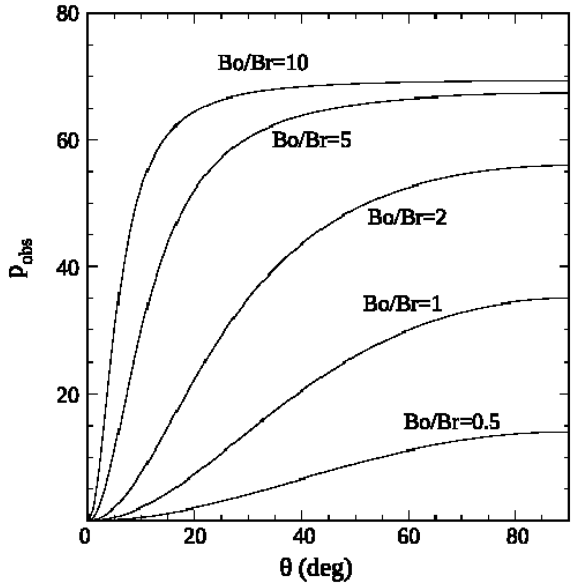

Figure 13. Observed fractional polarization as a function of the angle to the line of sight for different values of the ratio B_o/B_r and $p_{\rm int} = 70$ per cent.

fractional polarization can be achieved for large angles in agreement with what we obtain from the polarization images and from the roughly symmetric radio structure of these two radio galaxies.[2]

5.2 Multiple epochs of particle acceleration

The two arc-shaped structures observed in 3C 227 West and 3C 445 South may represent two shock fronts produced by the change of the jet direction on large scales, creating a dentist drill effect. On the other hand, the multiple compact components may trace the dithering of the jet termination point(s) interacting with an inhomogeneous backflow material on scale size up to 100 pc. The polarized clumps observed in the hotspots of 3C 227 and 3C 445 suggest the presence of multiple shocks that compress and align the magnetic field. A similar result was found for the southern hotspot in 3C 205 (Lonsdale & Barthel 1998). These clumps may trace the variation of the termination point of a dithering jet, as it was suggested by Tingay et al. (2008) for the hotspot of Pictor A, or they may represent the highest brightness temperature regions of a wide termination shock front with complex geometry. Determining the hotspot structure may improve our knowledge of the high-energy emission in these regions.

Compact and transient regions may be able to produce synchrotron emission up to X-rays. The spatial displacement between the X-ray emission and the radio-to-optical emission challenges the SSC and the inverse Compton (IC) scattering off cosmic microwave background (CMB) photons as the mechanisms responsible for the X-ray emission (Perlman et al. 2010; Hardcastle et al. 2007; Migliori et al., in preparation). IC emission is responsible for the X-ray emission in several hotspots and jet knots where the X-ray emission and the radio-to-optical emission are cospatial (see e.g. Kataoka & Stawarz 2005; Stawarz et al. 2007; Werner et al. 2012; Zhang et al. 2018). On the other hand, the misaligned X-ray emission may be produced by compact regions of the shock front that are currently accelerating particles, while the other shock fronts, that are traced by radio-to-optical emission, mark the location of previous epochs of acceleration. In fact, in the presence of magnetic field strength typical of these hotspots (40–150 μG, Brunetti et al. 2003; Migliori et al., in preparation), the lifetime of particles emitting in X-rays is about a few hundred years. This is marginally consistent with the average diffusive time of the particles in regions with 100 pc in size. The expected size of these compact and transient features emitting in the X-rays should be of the order of several tens of parsecs, i.e. comparable or a bit smaller than the size proved by these VLA observations. Migliori et al. (in preparation) show that the X-rays could result from the integrated synchrotron emission of several compact regions, and the radio emission of each single component is below the detection limit at 22 GHz.

The radiative lifetime of particles emitting in the optical band is of the order of 10^4 yr, comparable to the average diffusive time. Optical emission from relatively old shocks is supported by the VLT detection of the double arc-shaped structure in 3C 445 South and possibly in 3C 227 West. Optical emission on kpc scale may be also produced by turbulence, in agreement with low polarization level observed in some regions. The highly polarized subcomponents in which the kpc-scale arc-shaped structures are resolved indicates also the presence of strong shock acceleration occurring in different regions and at different time. The lack of X-ray emission cospatial with the radio-to-optical emission strongly supports this scenario. Multi-epoch deep X-ray observations are crucial for investigating flux variability and its time-scale, from months to years, which in turn would provide us with an estimate of the size of the regions responsible for the X-ray emission.

6 SUMMARY

In this paper, we presented results on subarcsecond polarimetric VLA observations at 22 GHz of the hotspots of the radio galaxies 3C 227 and 3C 445. The conclusions we can draw from this investigations are:

[2]For an organized field, a low level of polarization ($p < 40$ per cent) can be achieved only for small angles to the line of sight, $\theta < 10^\circ - 15^\circ$, which is unlikely for these objects.

(i) The hotspots 3C 227 West and 3C 445 South are characterized by a double arc-shaped structure, likely indicating two shock fronts.

(ii) In all the hotspots, the main components are resolved into several highly polarized compact clumps, with observed fractional polarization that may reach values as high as 70 per cent. The upper limit to their size is about 70–100 mas, corresponding to about 75–160 pc. Their flux density constitutes about 10 per cent of the whole hotspot region, indicating that the majority of the emission is on larger scales.

(iii) In all the hotspots, the highly polarized compact regions are embedded in the larger diffuse hotspot region, which is characterized by a much lower polarization, about 30–45 per cent on average, indicating significant random magnetic field component.

(iv) Although the total intensity emission and the polarized emission are both patchy, their morphology may be different (e.g. 3C 445 North). In general, there seems to be a displacement between the peaks of total intensity and the peaks of polarized emission, similar to what was already observed in ALMA observations of 3C 445 South.

(v) In 3C 227 West and in 3C 445 South, the X-ray emission and the radio emission are not cospatial and the main radio component is in agreement with the edge of the X-ray emission. The misalignment is difficult to reconcile with the SSC and IC-CMB model, but it may be explained by a population of highly energetic synchrotron emitting particles. Owing to their short radiative lifetime, X-ray emitting electrons should mark the region where particle acceleration is currently taking place, while radio-to-optical emission is detectable in older front shocks.

These observations support a scenario in which shocks from a dithering jet and turbulence are responsible for particle acceleration up to high energies. The highly polarized compact regions, less than 100 pc in size, resolved in these observations may represent the local multiple particle reaccelerators. No statistical studies on the (sub-)parsec scale of hotspots have been performed so far, and polarimetric high-resolution observations of a large number of hotspots is required to assess the complex structure of these regions and their acceleration mechanisms.

ACKNOWLEDGEMENTS

We thank the anonymous referee for reading the manuscript carefully and making valuable suggestions. FD acknowledges financial contribution from the agreement ASI-INAF no. 2017-14-H.0. This work was partially supported by the Korea's National Research Council of Science & Technology (NST) granted by the International joint research project (EU-16-001). The VLA is operated by the US National Radio Astronomy Observatory which is a facility of the National Science Foundation operated under cooperative agreement by Associated Universities, Inc. This work has made use of the NASA/IPAC Extragalactic Database (NED) which is operated by the JPL, Californian Institute of Technology, under contract with the National Aeronautics and Space Administration. This research has made use of SAOImage DS9, developed by the Smithsonian Astrophysical Observatory (SAO). Part of this work is based on archival data, software or online services provided by ASI Science Data Center (ASDC). This research has made use of software provided by the Chandra X-ray Center (CXC) in the application packages CIAO and CHIPS.

REFERENCES

Beck R., Berkhuijsen E. M., Uyaniker B., 1999, in Ostrowski M., eds, Proc. Int. Conf. Plasma Turbulence and Energetic Particles in Astrophysics. Reinhard Schlickeiser, Obserwatorium Astronomiczne, Uniwersytet Jagielloński, Cracow (Poland), p. 5
Black A. R. S., Baum S. A., Leahy J. P., Perley R. A., Riley J. M., Scheuer P. A. G., 1992, MNRAS, 256, 186
Brunetti G., Mack K.-H., Prieto M. A., Varano S., 2003, MNRAS, 345L, 40
Burn B. J., 1996, MNRAS, 133, 67
Carilli C. L., Kurk J. D., van der Werf P. P., Perley R. A., Miley G. K., 1999, AJ, 118, 2581
Fanaroff B. L., Riley J. M., 1974, MNRAS, 167, 31
Fanti C., Pozzi F., Dallacasa D., Fanti R., Gregorini L., Stanghellini C., Vigotti M., 2001, A&A, 369, 380
Fruscione A. et al., 2006, Proc. SPIE Conf. Ser. Vol. 6270, Observatory Operations: Strategies, Processes, and Systems, SPIE, Bellingham
Gurvits L. I., Schilizzi R. T., Miley G. K., Peck A., Bremer M. N., Roettgering H., van Breugel W., 1997, A&A, 318, 11
Hardcastle M. J. et al., 2016, MNRAS, 455, 3526
Hardcastle M. J., Harris D. E., Worrall D. M., Birkinshaw M., 2004, ApJ, 612, 729
Hardcastle M. J., Croston J. H., Kraft R. P., 2007, ApJ, 669, 893
Harris D. E., Carilli C. L., Perley R. A., 1994, Nature, 367, 713
Harwood J. J. et al., 2017, MNRAS, 469, 639
Isobe N., Koyama S., Kino M., Wada T., Nakagawa T., Matsuhara H., Niinuma K., Tashiro M., 2017, ApJ, 850, 193
Kataoka J., Stawarz L., 2005, ApJ, 622, 797
Laing R. A., 1980, MNRAS, 193, 439
Leahy J. P., Black A. R. S., Dennett-Thorpe J., Hardcastle M. J., Komissarov S., Perley R. A., Riley J. M., Scheuer P. A. G., 1997, MNRAS, 291, 20
Lonsdale C. J., Barthel P. D., 1984, A&A, 135, 45
Lonsdale C. J., Barthel P. D., 1998, AJ, 115, 895
Mack K.-H., Prieto M. A., Brunetti G., Orienti M., 2009, MNRAS, 392, 705
McKean J. P. et al., 2016, MNRAS, 463, 3143
Meisenheimer K., Yates M. G., Röser H.-J., 1997, A&A, 325, 57
Mingo B. et al., 2017, MNRAS, 470, 2762
Orienti M., Prieto M. A., Brunetti G., Mack K.-H., Massaro F., Harris D. E., 2012, MNRAS, 419, 2338
Orienti M., Brunetti G., Nagai H., Paladino R., Mack K.-H., Prieto M. A., 2017, MNRAS, 469, L123
Perley R. A., Butler B. J., 2013a, ApJS, 204, 19
Perley R. A., Butler B. J., 2013b, ApJS, 206, 16
Perlman E. S., Georganopoulos M., May E. M., Kazanas D., 2010, ApJ, 708, 1
Polatidis A. C., Conway J. E., 2003, PASA, 20, 69
Prieto M. A., Brunetti G., Mack K.-H., 2002, Science, 298, 193
Skrutskie M. F. et al., 2006, AJ, 131, 1163
Stawarz Ł., Cheung C. C., Harris D. E., Ostrowski M., 2007, ApJ, 662, 213
Tingay S. J., Lenc E., Brunetti G., Bondi M., 2008, AJ, 136, 2473
Werner M. W., Murphy D. W., Livingston J. H., Gorjian V., Jones D. L., Meier D. L., Lawrence C. R., 2012, ApJ, 759, 86
Young A. J., Wilson A. S., Tingay S. J., Heinz S., 2005, ApJ, 622, 830
Zhang J., Du S.-S., Guo S.-C., Zhang H.-M., Chen L., Liang E.-W., Zhang S.-N., 2018, ApJ, 858, 27

This paper has been typeset from a TEX/LATEX file prepared by the author.